Vector part of optical activity probed with x-rays in hexagonal ZnO

2007 J. Phys.: Condens. Matter 19 156201

(http://iopscience.iop.org/0953-8984/19/15/156201)

J. Phys.: Condens. Matter **19** (2007) 156201 (18pp) doi:10.1088/0953-8984/19/15/156201

Vector part of optical activity probed with x-rays in hexagonal ZnO

José Goulon[1,6], Nicolas Jaouen[1], Andrei Rogalev[1], Fabrice Wilhelm[1], Chantal Goulon-Ginet[1], Christian Brouder[2], Yves Joly[3], Elena N Ovchinnikova[4] and Vladimir E Dmitrienko[5]

[1] European Synchrotron Radiation Facility, BP 220 F-38043 Grenoble, France
[2] Institut de Minéralogie et de Physique des Milieux Condensés, Universités Paris-VI et VII, 4 place Jussieu, BP 115, F-75252 Paris, Cedex 05, France
[3] Institut Néel, CNRS, Associé à l'Université J Fourier, Boite F, BP 166, F-38042 Grenoble, Cedex 9, France
[4] Physics Department of Moscow State University, R-119899 Moscow, Russia
[5] Institute of Crystallography, R-119333 Moscow, Russia

E-mail: goulon@esrf.fr

Received 12 January 2007, in final form 14 February 2007
Published 16 March 2007
Online at stacks.iop.org/JPhysCM/19/156201

Abstract

We discuss how measurements of x-ray circular intensity differentials (XCIDs) could be used to probe the Voigt–Fedorov vector part of optical activity (OA) due to electric dipole–electric quadrupole ($E1E2$) interferences. The first experiment was carried out on a single crystal of zincite (hexagonal ZnO: class *6mm*). XCID spectra were recorded in the x-ray resonant diffraction regime near the Zn K edge using the (300) reflection at Bragg angles near 45°. In the x-ray range, the effective operator responsible for the vector part of OA can be assigned to the vector product $\mathbf{L} \times \mathbf{\Omega}_L - \mathbf{\Omega}_L \times \mathbf{L} \propto \mathbf{n}$, in which $\mathbf{L}$ and $\mathbf{\Omega}_L$ are time-reversal odd operators associated with the orbital angular momentum and the orbital anapole respectively, whereas $\mathbf{n}$ is a true time-reversal even electric dipole. This is consistent with the pyroelectric properties of zincite crystals.

(Some figures in this article are in colour only in the electronic version)

1. Introduction

Unlike Faraday rotation or magnetic circular dichroism (MCD), which refer mostly to electric dipole ($E1E1$) polarizabilities, *natural* optical activity (OA) is associated with transition probabilities that mix multipole moments of *opposite* parities, e.g. $E1M1$ or $E1E2$ [1–3]. The Curie's principle teaches us that this is only possible in systems with *odd* space parity. Since the discovery by Arago [4] and Biot [5], early in the 19th century, that crystalline quartz induced

[6] Author to whom any correspondence should be addressed.

Table 1. Irreducible parts of OA in O(3) [17].

Odd parity		Pseudo-scalar	Polar vector	Pseudo-deviator
Crystal classes	Point groups	Enantiomorphism	Voigt/Fedorov	**XNCD**
$\bar{4}3m$ $\bar{6}m2$ $\bar{6}$	T_d D_{3h} C_{3h}	−	−	−
432 23	O T	+	−	−
622 32 422	D_6 D_3 D_4	+	−	+
$6mm$ $3m$ $4mm$	C_{6v} C_{3v} C_{4v}	−	+	−
6 3 4	C_6 C_3 C_4	+	+	+
$\bar{4}2m$	D_{2d}	−	−	+
$\bar{4}$	S_4	−	−	+
$mm2$	C_{2v}	−	+	+
222	D_2	+	−	+
2	C_2	+	+	+
m	C_s	−	+	+
1	C_1	+	+	+

a rotation of the polarization vector of a linearly polarized light, OA has fascinated successive generations of physicists [6]. In the x-ray range, OA has long been ignored because the $E1M1$ interference terms, which dominate natural OA at optical wavelengths, become vanishingly small in x-ray absorption spectroscopy (XAS) given that, for deep inner-shell spectroscopies, magnetic dipole ($M1$) transitions are forbidden, at least in non-relativistic theories.

In the x-ray regime, however, the $E1E2$ cross terms become much stronger than at optical wavelengths and are at the origin of the rather large x-ray natural circular dichroism (XNCD) signatures which were measured at the ESRF in a variety of non-centrosymmetric crystals [7–12]. Table 1, which was first established by Jerphagnon and Chemla [17], is useful to clarify which ones among the 21 classes of non-centrosymmetric crystals may exhibit XNCD [13–16]. Following Landau–Lifshitz [18], OA is introduced as a consequence of spatial dispersion in the formulation of the electric induction [17]: $\mathcal{D} = \epsilon_{\mathcal{D}}\mathbf{E} + \eta\boldsymbol{\nabla} \otimes \mathbf{E}$, in which $\epsilon_{\mathcal{D}}$ is the permittivity tensor. If $\boldsymbol{\nabla} \otimes \mathbf{E}$ stands here for the tensor product of vectors ∇ and $\mathbf{E}$, then η is a third rank tensor characterizing optical activity (OA). We are concerned in this paper with the decomposition of η into irreducible representations invariant under the operations of the rotation group O(3). Crystal classes which admit a *pseudo*-deviator as rotational invariant are those which exhibit XNCD. Recall that XNCD was successfully measured in a biaxial crystal of potassium titanyl phosphate (KTP), which belongs to the *non*-enantiomorphous class $mm2$ [11, 12], for which η has no scalar part. Anyhow, the $E1E2$ tensors are traceless, i.e. have no *pseudo*-scalar part: this is consistent with the orthogonality of the spherical harmonics Y_1^m and Y_2^m which are commonly used to describe the electric dipole and electric quadrupole in O(3). As a practical consequence, XNCD vanishes in isotropic liquid phases even though it was found to be measurable in oriented liquid crystals [16].

In this paper, we wish to focus on crystals in which η has an irreducible part that transforms as a *polar vector* in O(3). Such crystals may exhibit no enantiomorphism nor any natural circular dichroism. In 1905, Voigt was the first to try to detect such a highly peculiar OA: his idea was that, in crystals of suitable symmetry, a linearly polarized incident light could be *reflected* as an elliptically polarized light [19]. This problem was reconsidered later by Fedorov [20], who suggested specific geometries to maximize the amplitude of OA at optical wavelengths. To the best of our knowledge, the first successful experiment was reported only in 1978, by Ivchenko and his colleagues [21], who looked for OA in the exciton resonance region where OA effects are enhanced. In their first experiment they used a uniaxial crystal

of cadmium sulfide (CdS) with the wurtzite type of structure, but they pointed out later to the generality of their approach [22, 23]. In 1990, Graham and Raab described the propagation of light in anisotropic crystals using an extended multipole theory which included $E1E2$ and even higher order terms. They noted the possible existence of a *skew* polarization inside the crystal [24, 25]. Already 14 years earlier, Jerphagnon and Chemla [17] had pointed out that the vector part of OA was associated with a (very) weak *longitudinal* component of electrical polarization that was a specific property of all *pyroelectric* materials.

Our experiment in the x-ray regime was performed with a uniaxial single crystal of zincite (hexagonal ZnO) featuring the same wurtzite type of structure as in the experiment of Ivchenko and his colleagues. Recall that zincite was given as the model of a diatomic pyroelectric crystal [26]. In the x-ray regime, specular reflection occurs only at very grazing incidence and cannot be used to detect a vector-type OA just as at optical wavelengths: it is the aim of this paper to show that *coherent* x-ray scattering in a resonant diffraction regime, i.e. diffraction anomalous near edge structures (DANES), can give access to the vector part of OA in the x-ray range. In section 2, we review how to transpose the concept of circular intensity differential (CID) into the x-ray scattering regime. Section 3 focuses on instrumentation and measurements whereas the nature of the effective operator responsible for the vector part of x-ray detected optical activity (XDOA) is discussed in section 4, in which *ab initio* simulations of the measured effect are also reported.

2. X-ray circular intensity differentials

2.1. Specular reflection at optical wavelengths

Zincite (space group $P6_3mc$, No 186) belongs to the crystal classes $4mm$, $3m$ and $6mm$, that are often (improperly) quoted as *optically inactive* because such crystals do not induce any optical rotation or any circular dichroism. Actually, table 1 reminds us that crystals which belong to these classes should exhibit OA, but only of vector type. Graham and Raab [25, 27] confirmed that reflectivity measurements would allow us to access the gyrotropy properties of such crystals when the optic axis is perpendicular to the plane of incidence, i.e. when $\mathbf{c} \perp [\mathbf{k}, \mathbf{k_s}]$. In measurements on scattered light, one is most often interested in the *circular intensity differentials* (CIDs) defined as [2]

$$\mathrm{CID}^{(\sigma,\pi)} = \frac{I_s^{\mathrm{L}(\sigma,\pi)} - I_s^{\mathrm{R}(\sigma,\pi)}}{I_s^{\mathrm{L}(\sigma,\pi)} + I_s^{\mathrm{R}(\sigma,\pi)}}. \tag{1}$$

Hereafter, the (σ, π) superscripts will be specified only when a given linear polarization component of the scattered light (perpendicular or parallel to the scattering plane) is measured while the incident photons are either left (L) or right (R) circularly polarized. For scattering at 90°, $\mathrm{CID}^{(\sigma)}$ and $\mathrm{CID}^{(\pi)}$ refer to *polarized* or *depolarized* circular intensity normalized differences respectively. Notice that $\mathrm{CID}^{(\sigma)}$ is equivalent to a measurement of the degree of circularity of the light scattered at 90°, since, according to Barron [2], $\mathrm{CID}^{(\sigma)} = -P_3^{\mathrm{s}}$. Starting from the usual Jones reflection matrix,

$$\begin{pmatrix} E_s^{\pi} \\ E_s^{\sigma} \end{pmatrix} = \begin{bmatrix} r_{\pi\pi} & r_{\pi\sigma} \\ r_{\sigma\pi} & r_{\sigma\sigma} \end{bmatrix} \begin{pmatrix} E_i^{\pi} \\ E_i^{\sigma} \end{pmatrix}. \tag{2}$$

Graham and Raab derived the following expression of the CID ratio for measurements performed without any polarization analysis:

$$\mathrm{CID} = \frac{2\,\mathrm{Im}[r_{\pi\pi} r_{\pi\sigma}^* - r_{\sigma\sigma} r_{\sigma\pi}^*]}{r_{\pi\pi} r_{\pi\pi}^* + r_{\pi\sigma} r_{\pi\sigma}^* + r_{\sigma\pi} r_{\sigma\pi}^* + r_{\sigma\sigma} r_{\sigma\sigma}^*}. \tag{3}$$

To follow closely the notations of [25], let us define inside the crystal the wavevectors $\mathbf{k}'' = \mathbf{k}c/\omega$, c being the speed of light in vacuum, ω its frequency and μ_0 the vacuum permeability whereas the refractive index (phase velocity index) is $n = |\mathbf{k}''|$. Inside such an anisotropic medium, two waves labelled $\{e, o\}$ are expected to propagate, which will differ by their components: ${k''_{ez}}^2 = n_e^2 - k''^2_x$ and ${k''_{oz}}^2 = {n_o}^2 - k''^2_x$. Here, $n_e = n_y$ and $n_o = n_x = n_z$ are the anisotropic refractive index components, whereas $k''_x = n\cos\theta_s$ satisfies the Snell–Descartes law.

When $\mathbf{c} \perp [\mathbf{k}, \mathbf{k_s}]$, there are non-vanishing off-diagonal Fresnel amplitudes that are responsible for gyrotropy:

$$r_{\pi\sigma} = r_{\sigma\pi} = \pm A_3 \frac{\mathrm{i}\cdot\mu_0 c n^2 \sin 2\theta_s}{(n\sin\theta_s + k''_{ez})(n_o^2\sin\theta_s + nk''_o z)}. \tag{4}$$

The CID ratio given in equation (3) will not vanish if $r_{\pi\sigma} = r_{\sigma\pi} \neq 0$ and simultaneously $r_{\pi\pi} \neq r_{\sigma\sigma}$. The latter condition is *a priori* satisfied since

$$r_{\pi\pi} = \frac{n_o^2\sin\theta_s - nk''_{oz}}{n_o^2\sin\theta_s + nk''_{oz}} \neq \frac{n\sin\theta_s - k''_{ez}}{n\sin\theta_s + k''_{ez}} = r_{\sigma\sigma}. \tag{5}$$

Thus, we are left with the condition $A_3 \sin 2\theta_s \neq 0$. The formulation of A_3 given by Graham and Raab is the same for crystal classes $4mm$, $3m$ and $6mm$ and includes terms related to the real part (Re) of the complex $E1E2$ tensor [24]. Dropping the $E1M1$ terms which are small in the x-ray range, the relevant part of their result expressed in the symmetry axes $\{1, 2, 3\}$ of the crystal would reduce to $A_3 = \frac{1}{2}\omega(a_{113} - a_{311})$, in which, in the Barron–Gray gauge [28],

$$a_{\alpha,\beta\gamma} = a_{\alpha,\gamma\beta} = 2\hbar^{-1}\Delta v \sum_N \omega_{JN} Z_{JN} \mathrm{Re}[\langle J|E1_\alpha|N\rangle\langle N|E2_{\beta\gamma}|J\rangle] \tag{6}$$

whereas $\omega_{JN} = \hbar^{-1}(E_N - E_J)$ and $Z_{JN} = (\omega_{JN}^2 - \omega^2)^{-1}$. Given the latter formulation of A_3, it is tempting to build up an extended gyration tensor $\zeta''_{ijk} = \frac{1}{2}\omega(a_{ijk} - a_{kij})$ preserving the time-reversal even parity of the a_{ijk} but which would be antisymmetric in the permutation of the first and last suffixes so that $A_3 = \zeta''_{311} = -\zeta''_{113}$ with $\zeta''_{333} = 0 = \zeta''_{iki}$. Since ζ''_{ijk} now satisfies the same permutation symmetry properties as η_{ijk}, it should transform in the same way in O(3): its vector-type irreducible component should then be $2\zeta''_{311} = 2A_3$ for crystal classes $4mm$, $3m$ and $6mm$ [17].

Equation (4) makes it clear that the CID ratio should be maximum for $\theta_s = 45°$ but should vanish at normal incidence $\theta_s = 90°$. This is consistent with the lack of CD signal. Of direct interest to us is the property that $A_3 \to -A_3$ when the crystal is rotated by π about the z axis, i.e. about the normal to the crystal.

2.2. X-ray coherent resonant scattering regime

Even though the results established by Graham and Raab refer only to Maxwell equations and constitutive equations with proper boundary conditions, their extension into the x-ray coherent resonant scattering regime deserves special care. Key issues in x-ray diffraction are related to the anisotropy of the anomalous dispersion (AAD) or the anisotropic tensor susceptibility (ATS). Actually, the understanding of these questions has much progressed over the past 20 years thanks to major contributions by several groups: Templeton and Templeton [29–31], Kirfel *et al* [32–34], Finkelstein *et al* [35] and Dimitrienko *et al* [36–40]. One typical problem concerned the observation near an absorption edge of Bragg reflections forbidden by tabulated glide-plane or screw-axis extinction rules: the current interpretation is that, due to resonant interaction with x-rays, crystallographically equivalent atoms could become non-equivalent scatterers owing to some *local* potential anisotropy.

Even more puzzling was the discovery by Templeton and Templeton [30, 31] that, in crystals of potassium chromate (space group $Pnma$, No 62) and germanium (space group $Fd3m$, No 227), third-rank tensor terms contributed to large changes of intensities for weak or forbidden reflections near the Cr and Ge K edges respectively: it was suggested that resonant interaction could possibly involve $E1E2$ excitations at *non*-centrosymmetric sites. Making reference here to optical activity may look strange because these crystals are centrosymmetric and, thus, are not optically active in the usual sense: note that there is actually no contradiction with the theory of XNCD because the contribution of such $E1E2$ excitations simply vanishes in the forward scattering geometry ($\mathbf{k_s} = \mathbf{k}$) in which the theory of XNCD would hold true [14]. Apparently, Blume [41, 42] was the first to realize that resonant x-ray scattering would allow one to access to a new type of site-selective XDOA. At any non-centrosymmetric absorbing site, there is a finite third-rank tensor $[E1E2]_{\alpha,\beta\gamma}$ that is inherently symmetric in a permutation of indices (β, γ) but that is not necessarily *fully* symmetric: its decomposition into irreducible components may yield at most one symmetric rank-3 septor, one rank-2 deviator and three vectors (two of them having the same length) [43]. It is the aim of this paper to clarify which are the irreducible components that may contribute to XDOA [39] and more specifically to a non-vanishing CID ratio.

The observation by Lee *et al* of a resonantly excited forbidden (600) reflection in germanium [44] provides us with a good example where any reference to OA would be irrelevant. A first interpretation supported by band-structure calculations was that p–d hybridization in the conduction band of germanium would make $E1E2$ excitations possible [45]. According to table 1, the non-centrosymmetric cubic point group $\bar{4}3m$ at the Ge sites is strictly *optically inactive*. Nevertheless, the third-rank $E1E2$ tensor has a fully symmetric irreducible septor (with only one single independent component): the latter may well contribute to resonant anomalous scattering [40] but not to XDOA. Another mechanism was alternatively proposed, whereby a third-rank anisotropy tensor could also arise from small, correlated vibrational displacements from the nominal sites of high symmetry [39, 46, 47]: such atomic displacements directly affect the electric dipole polarizability tensor ($E1E1$) and can contribute to a quite significant temperature-dependent correction to the scattered intensity. As detailed in [47], the so-called thermal motion induced (TMI) third-rank anisotropy tensor should have $3m$ symmetry and be symmetric in the permutation of (α, β) indices: its irreducible representations thus include two vectors both directed along **c** and one symmetric septor. To observe the (006) glide-plane forbidden reflection, further symmetry considerations suggest that fully symmetric representations of the anisotropy tensor are needed that cannot contribute to XDOA.

As pointed out by Voigt, a linearly polarized x-ray beam will be scattered as an elliptically polarized beam if and *only* if the $E1E2$ tensor has a non-vanishing polar vector-type irreducible component. Typically, this should not be the case with the glide-plane forbidden reflections in germanium. This statement was supported by a polarization analysis of the (006) reflection in azimuthal scans [48]: very little space was left for a (very weak) Stokes–Poincaré component P_3^s whenever the incident beam was linearly polarized. A fairly different situation could prevail for K_2CrO_4 because the point group at the non-centrosymmetric Cr sites (Wyckoff 4c positions) is now m, which, according to table 1, is compatible with a vector-type OA [17]: recent measurements at the ESRF have also confirmed that a linearly polarized incident x-ray beam was scattered as an elliptically polarized radiation [49].

The case of zincite was interesting because the space group of wurtzite let us expect glide-plane forbidden reflections of the type $(hh\ell)$ with $\ell =$ odd but $h \neq 0$. This prompted Collins *et al* [51] to study the resonantly excited forbidden reflection (115). Given that the point group symmetry of the zinc scattering atoms at the Wyckoff (a) sites is $3m$, antisymmetric $E1E2$

terms could possibly contribute here to a vector-type XDOA. On the other hand, ZnO has a low-lying optical phonon mode of energy 12.4 meV at the Γ-point [50]. There is now the difficulty that, in hexagonal ZnO, both $E1E2$ and TMI mechanisms yield third-rank anisotropy tensors referring to the same point group symmetry $3m$. The assumption made in [51] was that the two mechanisms had different temperature dependences: this led Collins *et al* to record the intensity of the (115) reflection as a function of energy (E) in the Zn near edge region on increasing the temperature from 59 to 800 K. The intensity of the forbidden reflection was then fitted according to a semi-empirical law [46, 51]:

$$I(E) = \left| A(E)\mathrm{e}^{\mathrm{i}\phi(E)} + B(E)\coth\left(\frac{\hbar\omega_0}{2kT}\right)\right|^2 \mathrm{e}^{-2M} \tag{7}$$

in which the temperature independent first term was tentatively assigned to the $E1E2$ contribution. Unfortunately, no information regarding XDOA could be obtained because only fully symmetric parts of the $E1E2$ or TMI anisotropy tensors make the observation of the (115) glide-plane forbidden reflection possible exactly as in the case of Ge.

Our strategy complements that adopted in [51]. Let us emphasize that the (300) reflection which we selected is *not* a forbidden reflection: on the contrary, it is quite strong and about 80% of its intensity is due to Zn atoms with $3m$ site symmetry. Moreover, what was measured was not simply the reflection intensity but the x-ray (diffracted) circular intensity differential (XCID) analogue to the CID of equation (1). What led us to select the (300) reflection is actually the argument that the corresponding Bragg angle θ_s was very close to 43° near the Zn K edge (9665 eV): by analogy with equation (4), one may then expect the contribution of some antisymmetric part of the tensor $E1E2$ to be maximized. Finally, it was anticipated that the measured XCID should reverse its sign on rotating the crystal by $\psi = 180°$.

2.3. Anisotropic tensor susceptibility formalisms

If we neglect non-resonant and magnetic terms, the total elastic scattering amplitude is given by the Kramers–Heisenberg formula:

$$F = \boldsymbol{\epsilon}_\mathrm{s}^* \cdot \boldsymbol{\epsilon}\langle J|\mathrm{e}^{\mathrm{i}(\mathbf{k}-\mathbf{k}_\mathrm{s})\cdot\mathbf{r}}|J\rangle + \frac{1}{m}\sum_N \frac{\langle J|\boldsymbol{\epsilon}_\mathrm{s}^* \cdot \mathbf{P}\mathrm{e}^{-\mathrm{i}\mathbf{k}_\mathrm{s}\cdot\mathbf{r}}|N\rangle\langle N|\boldsymbol{\epsilon} \cdot \mathbf{P}\mathrm{e}^{\mathrm{i}\mathbf{k}\cdot\mathbf{r}}|J\rangle}{E_J - E_N + \hbar\omega + \mathrm{i}\gamma} \tag{8}$$

where $\hbar\omega$, $\mathbf{k}$ and $\boldsymbol{\epsilon}$ are the energy, wavevector and polarization vector of the incident x-ray beam, $\mathbf{k}_\mathrm{s}$ and $\boldsymbol{\epsilon}_\mathbf{s}$ are the wavevector and polarization vector of the scattered x-ray beam, $\mathbf{P} = -\mathrm{i}\hbar\nabla$ and m is the electron mass. Note that we used the 'electrodynamics' convention for the phase of time evolution ($\mathrm{e}^{-\mathrm{i}\omega t}$), whereas within the 'crystallographer's' convention all scattering factors should be replaced by their complex conjugates. In a crystal, each point $\mathbf{G}$ of the Bravais lattice will add its own contribution $F(\mathbf{G})$. The term $F(0)$ is to be expanded as a sum over all sites n of the unit cell: $F(0) = \sum_n \mathrm{e}^{\mathrm{i}\mathbf{q}\cdot\mathbf{r}_n} f_n$, where $\mathbf{r}_n$ is the position of site n, $\mathbf{q} = \mathbf{k} - \mathbf{k}_\mathrm{s}$ is the scattering vector and f_n is the scattering factor for site n. Recall that f_n is the sum of multipole terms: $f_n = f_{n\mathrm{T}} + f_{n\mathrm{dd}} + f_{n\mathrm{dq}} + f_{n\mathrm{qq}} + \cdots$. Here $f_{n\mathrm{T}}$ denotes the Thomson scattering contribution: $f_{n\mathrm{T}} = (\boldsymbol{\epsilon}_\mathbf{s}^* \cdot \boldsymbol{\epsilon})\, f_0$ where $f_0 = \langle I|\mathrm{e}^{\mathrm{i}\mathbf{q}\cdot\mathbf{r}}|I\rangle$ is real; $f_{n\mathrm{dd}}$ is the dipole–dipole contribution, $f_{n\mathrm{dq}}$ is the dipole–quadrupole contribution and $f_{n\mathrm{qq}}$ the quadrupole–quadrupole contribution. To simplify notation, we shall drop hereafter the site index n.

To take into account polarization, we introduce now the scattering factors $f^{\sigma\sigma}$, $f^{\sigma\pi}$, $f^{\pi\sigma}$ and $f^{\pi\pi}$, in which the two superscripts refer to the linear polarization states of the incident and scattered beams respectively. Left/right-circular polarization states of the incident beam will be described using the complex polarization vectors: $\boldsymbol{\epsilon} = (\epsilon^\pi \pm \mathrm{i}\epsilon^\sigma)/\sqrt{2}$, so that $f^{\mathrm{L/R}\sigma} = (1/\sqrt{2})(f^{\pi\sigma} \pm \mathrm{i}f^{\sigma\sigma})$ and $f^{\mathrm{L/R}\pi} = (1/\sqrt{2})(f^{\pi\pi} \pm \mathrm{i}f^{\sigma\pi})$. The total scattered

intensity corresponding to a right/left incident light is then

$$I^{\mathrm{L/R}} = I^{\mathrm{L/R},\sigma} + I^{\mathrm{L/R},\pi} = \frac{|f^{\pi\sigma} \pm \mathrm{i} f^{\sigma\sigma}|^2 + |f^{\pi\pi} \pm \mathrm{i} f^{\sigma\pi}|^2}{2} \tag{9}$$

whereas

$$\Delta I = I^{\mathrm{L}} - I^{\mathrm{R}} = -2\,\mathrm{Im}[f^{\sigma\sigma}(f^{\pi\sigma})^* + f^{\sigma\pi}(f^{\pi\pi})^*]. \tag{10}$$

One may easily check that

$$\begin{aligned} f^{\sigma\sigma} &= f_0 + f^{\sigma\sigma}_{\mathrm{dd}} + f^{\sigma\sigma}_{\mathrm{dq}} + f^{\sigma\sigma}_{\mathrm{qq}} \\ f^{\pi\sigma} &= f^{\pi\sigma}_{\mathrm{dd}} + f^{\pi\sigma}_{\mathrm{dq}} + f^{\pi\sigma}_{\mathrm{qq}} \\ f^{\sigma\pi} &= f^{\sigma\pi}_{\mathrm{dd}} + f^{\sigma\pi}_{\mathrm{dq}} + f^{\sigma\pi}_{\mathrm{qq}} \\ f^{\pi\pi} &= \cos 2\theta_{\mathrm{s}} f_0 + f^{\pi\pi}_{\mathrm{dd}} + f^{\pi\pi}_{\mathrm{dq}} + f^{\pi\pi}_{\mathrm{qq}} \end{aligned}$$

where θ_{s} is the Bragg angle. Let us keep in mind that the dominant terms are the Thomson and dipole–dipole contributions. Neglecting the quadrupole–quadrupole contributions we get

$$\begin{aligned} \Delta I \simeq\ & -2 f_0\,\mathrm{Im}(f^{\pi\sigma}_{\mathrm{dd}} + f^{\pi\sigma}_{\mathrm{dq}}) + 2\cos 2\theta_{\mathrm{s}} f_0\,\mathrm{Im}(f^{\sigma\pi}_{\mathrm{dd}} + f^{\sigma\pi}_{\mathrm{dq}}) \\ & + 2\,\mathrm{Im}[f^{\sigma\sigma}_{\mathrm{dd}}(f^{\pi\sigma}_{\mathrm{dd}})^* + f^{\sigma\sigma}_{\mathrm{dd}}(f^{\pi\sigma}_{\mathrm{dq}})^* + f^{\sigma\sigma}_{\mathrm{dq}}(f^{\pi\sigma}_{\mathrm{dd}})^* \\ & + f^{\sigma\pi}_{\mathrm{dd}}(f^{\pi\pi}_{\mathrm{dd}})^* + f^{\sigma\pi}_{\mathrm{dq}}(f^{\pi\pi}_{\mathrm{dd}})^* + f^{\sigma\pi}_{\mathrm{dd}}(f^{\pi\pi}_{\mathrm{dq}})^*]. \end{aligned}$$

Let us write explicitly the dipole–dipole and dipole–quadrupole contributions:

$$f_{\mathrm{dd}} = \sum_N \frac{m\omega_{JN}^2}{E_J - E_N + \hbar\omega + \mathrm{i}\gamma} \sum_{\alpha\beta} \epsilon^*_{\mathrm{s}\alpha}\epsilon_\beta d_{\alpha\beta}$$

$$f_{\mathrm{dq}} = (\mathrm{i}/2) \sum_N \frac{m\omega_{JN}^2}{E_J - E_N + \hbar\omega + \mathrm{i}\gamma} \sum_{\alpha\beta\gamma} \epsilon^*_{\mathrm{s}\alpha}\epsilon_\beta (t_{\alpha\beta\gamma}k_\gamma - t^*_{\beta\alpha\gamma}k_{\mathrm{s}\gamma})$$

in which $d_{\alpha\beta} = \langle J|r_\alpha|N\rangle\langle N|r_\beta|J\rangle$ and $t_{\alpha\beta\gamma} = \langle J|r_\alpha|N\rangle\langle N|r_\beta r_\gamma|J\rangle$, whereas $\omega_{JN} = (E_J - E_N)/\hbar$. In a non-magnetic crystal such as zincite, the wavefunctions $|J\rangle$ and $|N\rangle$ are time-reversal even, so that $d_{\alpha\beta}$ and $t_{\alpha\beta\gamma}$ are real. Indeed, we have the usual permutation symmetries: $d_{\beta\alpha} = d_{\alpha\beta}$ and $t_{\alpha\gamma\beta} = t_{\alpha\beta\gamma} \propto \mathrm{Re}[E1E2]_{\alpha\beta\gamma}$.

Moreover, for the space group $P6_3mc$, translations $\mathbf{r}_n$ within the unit cell are along the **c** axis whereas, in our experiment, the scattering vector is along $\mathbf{a}^*$ because the reflecting plane is (300). As a consequence: $\mathbf{q}\cdot\mathbf{r}_n = 0$ and the phase factor $\mathrm{e}^{\mathrm{i}\mathbf{q}\cdot\mathbf{r}_n} = 1$. This implies that the symmetry group that is relevant in the calculation of the scattering factors is no longer the local point group $3m$ ($\mathrm{C_{3v}}$) of the Zn sites, but the full point group of the crystal $6mm$ ($\mathrm{C_{6v}}$). This consideration led us to the following result:

$$\begin{aligned} \sum_{\alpha\beta\gamma} \epsilon^*_{\mathrm{s}\alpha}\epsilon_\beta (t_{\alpha\beta\gamma}k_\gamma - t_{\beta\alpha\gamma}k_{\mathrm{s}\gamma}) &= [(\boldsymbol{\epsilon}^*_{\mathbf{s}}\cdot\mathbf{k})\epsilon_3 - (\boldsymbol{\epsilon}\cdot\mathbf{k}_{\mathbf{s}})\epsilon^*_{\mathrm{s}3}]t_{113} \\ & + q_3[(\boldsymbol{\epsilon}^*_{\mathbf{s}}\cdot\boldsymbol{\epsilon})t_{113} + \epsilon^*_{\mathrm{s}3}\epsilon_3(t_{333} - t_{113} - t_{311})] \end{aligned} \tag{11}$$

where the **1** and **3** axes are along the **a** and **c** axes of the crystal, respectively, and the **2** axis is perpendicular to **1** and **3**. The first term is antisymmetric in $\boldsymbol{\epsilon}$ and $\boldsymbol{\epsilon}^*_{\mathbf{s}}$ and proportional to $\mathbf{k}+\mathbf{k}_{\mathbf{s}}$, as can be seen using the identity [54]

$$(\boldsymbol{\epsilon}^*_{\mathbf{s}}\cdot\mathbf{k})\boldsymbol{\epsilon} - (\boldsymbol{\epsilon}\cdot\mathbf{k}_{\mathbf{s}})\boldsymbol{\epsilon}^*_{\mathbf{s}} = (\boldsymbol{\epsilon}^*_{\mathbf{s}}\times\boldsymbol{\epsilon})\times(\mathbf{k}+\mathbf{k}_{\mathbf{s}}). \tag{12}$$

The second term of equation (11) is symmetric in $\boldsymbol{\epsilon}$ and $\boldsymbol{\epsilon}^*_{\mathbf{s}}$ and proportional to $\mathbf{q} = \mathbf{k} - \mathbf{k}_{\mathbf{s}}$. This second term, however, vanishes in our experiment because $q_3 = 0$, since **c** was set perpendicular to the scattering vector **q**. Thus, given the geometry of our experiment, the XCID ratio will depend only on one single dipole–quadrupole term, t_{113}: this is at variance with the result of Graham and Raab discussed in section 2.1.

The next step is to calculate the angular dependence of the various scattering factors during an azimuthal (ψ) rotation, especially when **c** is perpendicular to the scattering plane ($\psi = \pm\pi/2$). Regarding first $f_{\rm dd}$ and defining $g^{\epsilon\epsilon_{\rm s}} = \sum_{\alpha\beta} \epsilon^*_{{\rm s}\alpha}\epsilon_\beta d_{\alpha\beta}$, one obtains

$$\begin{aligned} g^{\sigma\sigma} &= \cos^2\psi d_{11} + \sin^2\psi d_{33}, \\ g^{\sigma\pi} &= -g^{\pi\sigma} = \sin\psi\cos\psi\sin\theta_{\rm s}(d_{33} - d_{11}), \\ g^{\pi\pi} &= (\cos^2\theta_{\rm s} - \sin^2\psi\sin^2\theta_{\rm s})d_{11} - \cos^2\psi\sin^2\theta_{\rm s} d_{33}. \end{aligned}$$

Note that $f_{\rm dd}^{\sigma\pi} = f_{\rm dd}^{\pi\sigma} = 0$ when $\theta_b = \pi/4$. The angular dependence of the dipole–quadrupole term is much simpler since $f_{\rm dq}^{\sigma\sigma} = f_{\rm dq}^{\pi\pi} = 0$ and

$$f_{\rm dq}^{\sigma\pi} = f_{\rm dq}^{\pi\sigma} = \sin\psi\sin 2\theta_{\rm s}({\rm i}/2)\sum_N \frac{m\omega_{JN}^2}{E_J - E_N + \hbar\omega + {\rm i}\gamma} t_{113}. \tag{13}$$

In our experiment, $\theta_{\rm s}$ is close to $\pi/4$ and the only term proportional to $\sin\psi$ is indeed the dipole–quadrupole contribution $-2f_0\,{\rm Im}(f_{\rm dq}^{\pi\sigma})$. Any other term has an angular dependence in $n\psi$ with $n > 1$.

Following the original work of Trammel *et al* [52], Carra and co-workers [53, 54] tried to exploit irreducible *spherical* tensors instead of irreducible Cartesian tensors. This approach proved to be most successful to identify the *effective* operators involved in the resonance process. In particular, Marri and Carra [54] reported recently a detailed analysis of the anisotropy tensors associated with $E1E2$ excitation for both time-reversal even and time-reversal odd processes ($\mathcal{R} = \pm 1$). The $E1E2$ contributions to the resonant scattering process could be linearly decomposed as

$$\begin{aligned} f_{E1E2} = (4\pi/k)\sum_{\kappa,q,\mathcal{R}} T_q^{(\kappa,\mathcal{R})*}(\boldsymbol{\epsilon}_{\mathbf{s}}^*, \mathbf{k}_{\mathbf{s}}; \boldsymbol{\epsilon}, \mathbf{k}) \sum_{\ell=\ell_c\pm1,\ell'=\ell\pm1} \mathcal{A}(\omega_{\mathbf{k}}) \\ \times \sum_{j,x}[\langle g|c_\kappa^{\mathcal{R}}\mathcal{O}_q^{(\kappa,\mathcal{R})}(\ell,\ell')_j + (-1)^\eta d_\kappa^{\mathcal{R}}\mathcal{S}_q^{(\kappa,\mathcal{R},x)}(\ell,\ell')_j|g\rangle] \end{aligned} \tag{14}$$

in which $\mathcal{O}_q^{(\kappa)}$ and $\mathcal{S}_q^{(\kappa)}$ are respectively spinless and spin-dependent operators of rank-κ expressed in terms of the electronic ground state $|g\rangle$. As in the case of absorption spectra [16], the complex tensors $T_q^{(\kappa,\mathcal{R})}$ are required to describe what coupling is possible with a given polarization state of the incident and of the scattered x-ray photons; $\mathcal{A}$ is a dimensionless scattering amplitude describing the resonant process. In our problem, equation (14) is expected to simplify considerably: since our experiments was carried out at a K-edge, only spinless operators ($\mathcal{O}$) should be considered; we are concerned here only with a time-reversal even process ($\mathcal{R} = +1$); finally, the effective operator should implicitly transform as a vector ($\kappa = 1$) and, according to [54] (see table 2), the only effective operator satisfying this requirement is $\mathbf{n} = \mathbf{r}/r$. Marri and Carra also identified two additional time-reversal even, spinless effective operators: the first one is the orbital *pseudo*-deviator involved in XNCD experiments; the second one is an octupolar operator most probably linked to the symmetric septor part of $E1E2$ and which seems to play the key role in the case of the germanium (006) forbidden reflection. This may not be true regarding the forbidden reflections ($hk0$, h odd) in potassium chromate because the point group symmetry of the Cr atoms in site 4(c) [30, 49] is m_y and not $\bar{4}3m$ as erroneously stated in [54]: irreducible representations of both vector and *pseudo*-deviator types may have then to be considered. Anyhow, as noticed by Marri and Carra, neither the dipolar nor the octupolar operator can be measured by an x-ray absorption experiment.

In a further attempt to get a deeper insight into the nature of the term t_{113} measured in a XCID experiment, let us examine first which are the irreducible components of the third rank tensor ${\rm Re}[E1E2]_{\alpha,\beta\gamma}$. For such a symmetric third rank tensor and point group symmetry

6*mm*, the decomposition into irreducible components carried out by Jerphagnon *et al* [43] confirms that there is no deviator and that the only components that survive are two vectors: $V_1 \propto [4t_{113} + t_{333}]$; $V_3 \propto [ta_{311} + t_{333}]$ plus a symmetric septor with non-zero terms: $S_{333} = 2(t_{333} - 3t_{311})/5$; $S_{311} = S_{322} = (3t_{311} - t_{333})/5$. It thus appears that t_{113} is unambiguously associated with a polar, vector-type irreducible representation of $\mathrm{Re}[E1E2]_{\alpha,\beta\gamma}$. If we look next at the spherical tensor analysis of the elastic scattering amplitude carried out by Marri and Carra [54], we find that, for 6*mm* symmetry, only the tensor components $\mathcal{P}_0^{(1,+)}$ (dipole) and $\mathcal{F}_0^{(3,+)}$ (octupole) do not vanish and their values are proportional to $3t_{113} - t_{311} + t_{333}$ and $-2t_{113} - t_{311} + t_{333}$, respectively. Thus t_{113} is found to contribute to both $\mathcal{P}_0^{(1)}$ and $\mathcal{F}_0^{(3)}$.

Following Buckingham and Raab [55], further simplification arises in systems with C_{3v} or C_{6v} symmetry since, according to Birss [56], $t_{333} = -2t_{311}$: as a consequence, $V_3 = 0$, $V_1 \propto [2t_{113} - t_{311}]$, whereas $S_{333} = -2S_{311} = -2S_{322} = -2t_{311}$. Similarly, one obtains $\mathcal{P}_0^{(1,+)} \propto 3[t_{113} - t_{311}]$, whereas $\mathcal{F}_0^{(3,+)} \propto -[3t_{311} + 2t_{113}]$. It now clearly appears that this is the dipole operator of the Marri–Carra $\mathcal{P}_0^{(1,+)}$, which should be proportional to the vector part of the OA tensor but not the XCID ratio itself. To determine unambiguously $\mathcal{P}_0^{(1,+)}$ and $\mathcal{F}_0^{(3,+)}$, one should complement the measurement of the XCID ratio with another experiment aimed at characterizing the fully symmetric septor part of $\mathrm{Re}[E1E2]$ that depends here on one single term: t_{311}.

3. Experimental XCID measurements

3.1. ESRF beamline ID12 and related instrumentation

The experiment was carried out at the ESRF beamline ID12. Since this beamline has been extensively described elsewhere [57, 58], only a few points will be considered that were determinant for this project. In changing the phase between the horizontal/vertical magnetic field arrays of our HELIOS-type helical undulator, we had the capability to flip the circular polarization of the emitted x-ray photons from left to right. Even though the Stokes–Poincaré circular polarization rate P_3 of the x-ray source exceeded 0.97, reverting the helicity of the undulator radiation unfortunately does not imply that, at the sample location, the helicity of the monochromatic photons will be perfectly inverted as well. This will happen only if

(i) the two-crystal monochromator is operated at a Bragg angle far from 45°, where the monochromator becomes itself a linear polarimeter, and
(ii) the Stokes–Poincaré component P_2 of the monochromatic x-ray beam is kept very small.

The KoHzu monochromator of beamline ID12 was equipped with a pair of Si(111) crystals cooled down to 140 K. Owing to the fact that the DANES spectra were recorded at the Zn photoionization K edge (9.659 keV), no low-pass mirror was required to cut harmonics and no focusing optics was needed. With a Bragg angle (θ_B) of the order of 11.8°, the intrinsic energy resolution of the monochromator was not particularly impressive ($\Delta E = 1.72$ eV), but on closing the slits located in front of the diffractometer we reduced further the vertical divergence to 4.3 μrad and improved the energy resolution to 1.38 eV. For such a small Bragg angle, we could check that the circular polarization rate of the monochromatic beam was very high, with $P_2 \leqslant 0.02$.

For this experiment, we did not use a sophisticated multicircle diffractometer: we simply adapted a UHV reflectometer initially designed for other purposes [59, 60]. In the configuration illustrated with figure 1, a UHV compatible six-way port stainless-steel chamber could be rotated about a horizontal axis (Y) perpendicular to the diffraction plane [X, Z] defined with respect to the laboratory frame {X, Y, Z}. Note that {x, y, z} is the reference frame of the

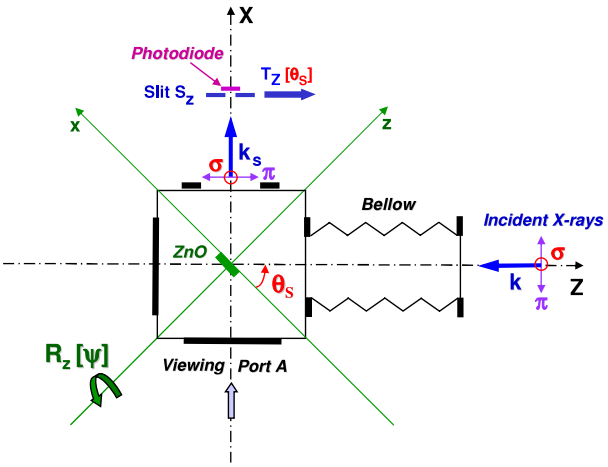

Figure 1. Geometry of the XCID experiment and schematic view of the diffractometer. Notice that the crystal **c** axis is perpendicular to the scattering plane for $\psi = \pm\pi/2$.

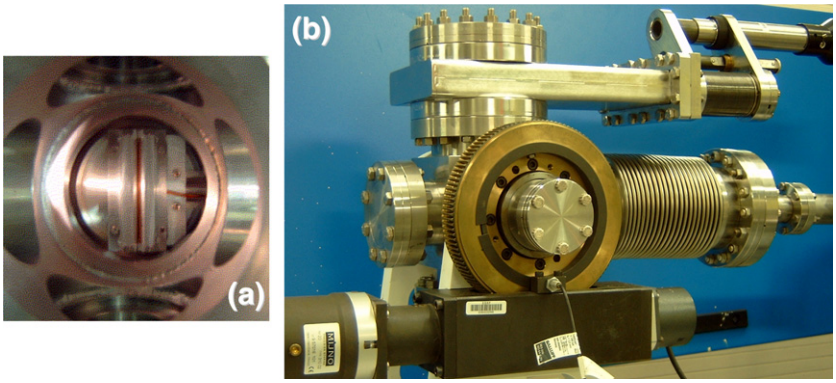

Figure 2. *In vacuum* diffractometer: (a) detector/slit assembly seen from viewing port A; (b) overall view of the diffractometer with its rotating chamber and playless wormscrew.

sample, not to be confused with the symmetry axes of the crystal. A fine tuning of rotation ΔR_Y was required to scan the rocking-curve profile of the selected reflection: this was possible thanks to a very high-precision playless helical wormscrew (Zahnradfabrik OTT, Germany), which allowed us to rotate the whole chamber whereas two differentially pumped rotary drives preserved the full UHV compatibility of the rotating vessel (see figure 2(b)). Since the orientation of the crystal was basically defined by the geometry of the sample holder, the amplitude of ΔR_Y did not exceed in practice a few degrees and the input bellow could perfectly accommodate mechanically such a small adjustment of the Bragg angle (θ_s), that was performed with an angular resolution of about ± 1.5 μrad.

In this experiment, we were concerned with Bragg angles of the order of $\theta_s \simeq 45°$. The detector had then to be located along the $2\theta_s$ direction, i.e. at about 90° from the incident beam or close to the vertical (X) axis. For convenience, the 2θ scan was replaced by a trivial translation (T_Z) of a narrow slit ($\delta S_Z \simeq 0.5$ mm) (see figure 2(a)) located in front of the detector at about 14 cm of the sample. The detector was a low-noise photodiode manufactured

by Eurisys-Canberra (France) and fully compatible with the standard readout electronics in use on beamline ID12. Its size ($L_Y = 70$ mm; $L_Z = 12$ mm) did help us to make the whole experiment much less sensitive to lateral (angular) instabilities of the incident x-ray beam but, unfortunately, it also increased the fluorescence background, even though the narrow slit did considerably restrict the solid angle over which fluorescence photons were collected. An azimuthal rotation ($\Delta\psi$) about the sample axis (z) was implemented using a compact, in-vacuum stepper motor (Caburn MDC) attached to the sample holder. In order to carefully align the diffractometer with respect to the incident beam, two more degrees of freedom were required: a transverse translation T_Y and a rotation R_X around the vertical axis.

3.2. Data acquisition and data reduction

A high-quality single crystal of zincite was purchased from Escete (Enschede, Netherlands). This crystal platelet (5 mm × 10 mm × 2 mm) was cut with its optic **c** axis parallel to the 10 mm long edge. The Bragg reflections were found to agree rather well with the literature parameters [26]: $a = b = 3.2499$ Å; $c = 5.2066$ Å; volumic mass $\rho = 11.3138$ g cm^{-3}. For the (300) reflection ($2d = 1.8763$ Å), the Bragg angle decreased from 43.19° to 42.75° over the selected Zn K-edge XANES range (9654.6–9734.7 eV). At the beginning of each experiment, the alignment of the diffractometer was systematically checked and the location of the detector assembly (photodiode + slit) was carefully optimized in order to avoid any further translation (T_Z) during a whole energy scan of the monochromator. For each energy setting (θ_B) of the monochromator, a rocking curve of the zincite (300) reflection was recorded first with left circular polarization, and immediately afterwards with right circular polarization. To achieve an accurate definition of the reflection tails, each θ_s scan included 101 data points with an average incremental rotation $\Delta\theta_s = -0.002°$ (i.e. 34.9 μrad). Under the present experimental conditions, the angular width of the reflection was of the order of about 50 arcsec (FWHM). Unfortunately, the accuracy of the azimuthal rotation ($\Delta\psi$) was not as good and, in the absence of any angular encoder, the reproducibility of a given angular setting hardly exceeded 0.2°.

Data reduction was performed with a modified Fortran package (danes) adapted from an existing one (xanes), which was previously developed to analyse XNCD as well as a variety of non-reciprocal x-ray dichroisms [16, 61]. The maximum peak intensity or the measured area under each reflection were only used as starting parameters to refine the analysis of the rocking curve using a Voigt profile in which the expected Lorentzian lineshape was convoluted with a Gaussian broadening function. Simultaneously, the background was decomposed on a (truncated) orthogonal basis of low-order Tchebychev polynomials. Global fits were generated on adapting to the present task the powerful minimization package *MINUIT* from CERN [62] which includes error analyses and covariance matrix calculations for a safe fitting practice. The results of the fits generated for each energy and each circular polarization were then combined together to produce finally a variety of spectra:

- the polarization averaged DANES spectrum $\frac{1}{2}[I_s^L(E) + I_s^R(E)]$;
- the polarization averaged, deconvoluted Lorentzian angular width $WL(E)$;
- the asymmetry factor $g(\mathrm{XCID}) = 2 * [I_s^L(E) - I_s^R(E)]/[I_s^L(E) + I_s^R(E)] = 2 * \mathrm{XCID}$.

Recall that all diffracted intensities (I_s) were systematically normalized with respect to a signal proportional to the incident intensity (I_0). Regarding XCID spectra, let us make it clear that we did not resolve the two linear polarization components of the diffracted beam. However, since $2\theta_s \simeq 90°$, the only additional contribution to be taken into account is from *depolarized* x-ray photons [2], but the latter contribution is expected to be small.

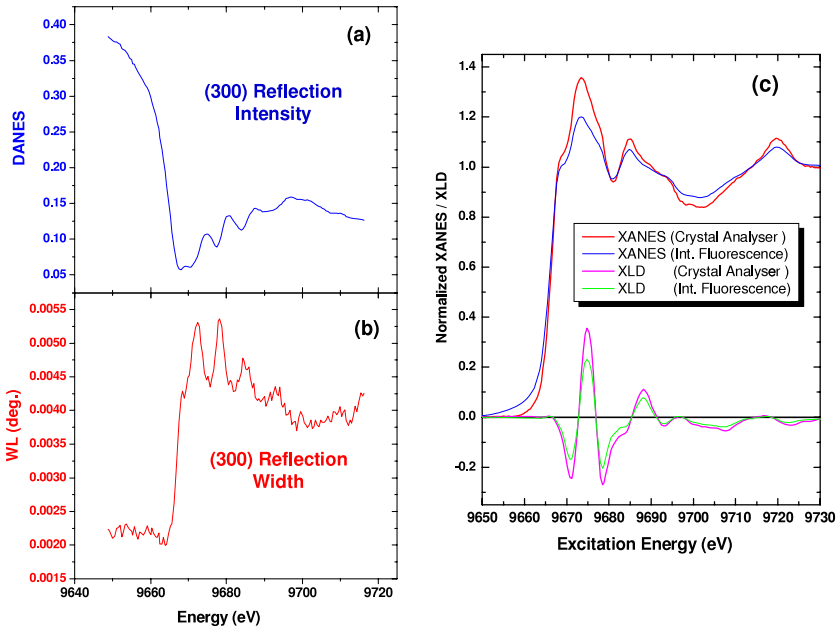

Figure 3. DANES (a) and WL (b) spectra of the (300) reflection of zincite recorded with $\mathbf{c} \perp [\mathbf{k}, \mathbf{k_s}]$ and $\psi = -\pi/2$. The DANES signal was not corrected for absorption. Polarization averaged XANES and XLD spectra are reproduced as references in plot (c); note the enhanced resolution achieved in the RIXS detection mode.

We have reproduced in figure 3(a) the DANES spectrum of the (300) reflection measured in a geometry in which the optic axis of the ZnO crystal was set perpendicular to the plane of incidence, i.e. with $\mathbf{c} \perp [\mathbf{k}, \mathbf{k_s}]$ and $\psi = -\pi/2$. The raw data displayed in figure 3(a) were not corrected for absorption because such a correction will cancel out in the calculation of the XCID ratio. We have also displayed in figure 3(b) the reflection width spectrum $WL(E)$. Obviously the two spectra shown in figures 3(a) and (b) are different and it seems that the spectrum $WL(E)$ reproduces the XANES signatures with a better contrast. Recall that $WL(E) \propto f''(E)$ and near edge oscillations have already been measured in this way in the soft x-ray range [63]. What may not be so well recognized, especially among hard x-ray spectroscopists, is the property that the very weak $WL(E)$ signatures benefit from an enhancement due to the virtual absence of core–hole broadening within the adiabatic approximation of the scattering process. This point will be considered in more detail elsewhere.

For the sake of reference, we found it useful to reproduce in figure 3(c) polarization averaged XANES spectra and *natural* x-ray linear dichroism (XLD) spectra recorded independently with the same zincite crystal and $\mathbf{c} \perp [\mathbf{k}, \mathbf{k_s}]$. The XLD spectra were measured on inserting downward with respect to the monochromator a quarter-waveplate (QWP) to convert the monochromatic, circularly polarized x-ray photons into linearly polarized x-ray photons with either σ or π polarization. Note that all XANES or XLD spectra were recorded in the fluorescence excitation mode either on monitoring the integrated emission of the backscattered fluorescence intensity or on using a high-resolution crystal analyser as described in more detail in [64]. As expected, the spectra recorded with the crystal analyser were found to benefit from an enhanced energy resolution of the XANES signatures because the core–hole broadening was again significantly reduced.

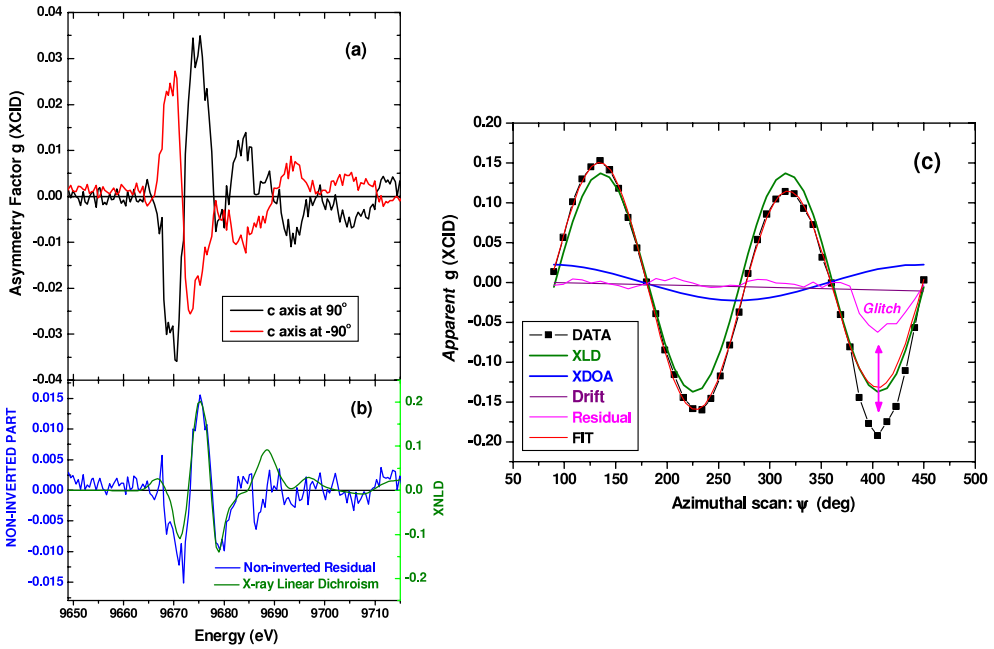

Figure 4. (a) Asymmetry factor of the (300) reflection of zincite measured with $\mathbf{c} \perp [\mathbf{k}, \mathbf{k_s}]$ and $\psi = \pm\pi/2$; (b) non-inverted part of the asymmetry factor spectra compared to a rescaled XLD spectrum; (c) fit of the azimuthal scan performed at a fixed energy (9675 eV) where XDOA measured at $\psi = \pi/2$ was maximum; an unwanted glitch is marked with an arrow.

3.3. Measured XCID spectra

The spectral dependence of the asymmetry factor g(XCID) of the (300) reflection of zincite has been measured first with $\mathbf{c} \perp [\mathbf{k}, \mathbf{k_s}]$ and is displayed in figure 4(a) for $\psi = \pm\pi/2$. These spectra confirm that there is a component that is nicely inverted when the azimuthal angle is rotated by 180°: this component is to be assigned to the vector part of XDOA. Nevertheless, there is also a small residual signal that is not inverted and is shown in figure 4(b) to reproduce—with some scaling factor—the *natural* x-ray linear dichroism (XLD) spectrum arising from pure electric dipole ($E1E1$) polarizabilities. Ideally, the crystal should have been rotated about the scattering vector $\mathbf{q} = \mathbf{k} - \mathbf{k_s}$ but the mechanical design of our diffractometer allowed us to rotate it only about the z axis, which is not strictly normal to the diffracting planes. This approximation could explain part of the *non-inverted* (residual) signal. On the other hand, in the absence of any absolute calibration of the azimuthal angle ψ, we cannot pretend that the crystal was strictly oriented at $\psi = \pm 90°$ with an accuracy better than 0.1°.

We found also interesting to study at a fixed energy the angular dependence of the *apparent* asymmetry factor during an azimuthal scan. The result is shown in figure 4(c), which reproduces the angular dependence of g(XCID) when the energy of the incident x-ray photons was tuned to the energy of the maximum XCID signal measured at $\psi = 90°$. Obviously, we do not observe the angular dependence ($\propto \sin\psi$) that one would expect for a pure XDOA contribution: the measured angular dependence is merely $\propto \sin 2\psi$ as observed in any common x-ray linear dichroism (XLD) experiment. Actually, only a Fourier decomposition of the whole signal by appropriate numerical methods (FT or least-square fit) makes it possible to disentangle the respective contributions of XDOA and natural XLD. This is illustrated with figure 4(c), in which we reproduced the individual contributions of XDOA and XLD

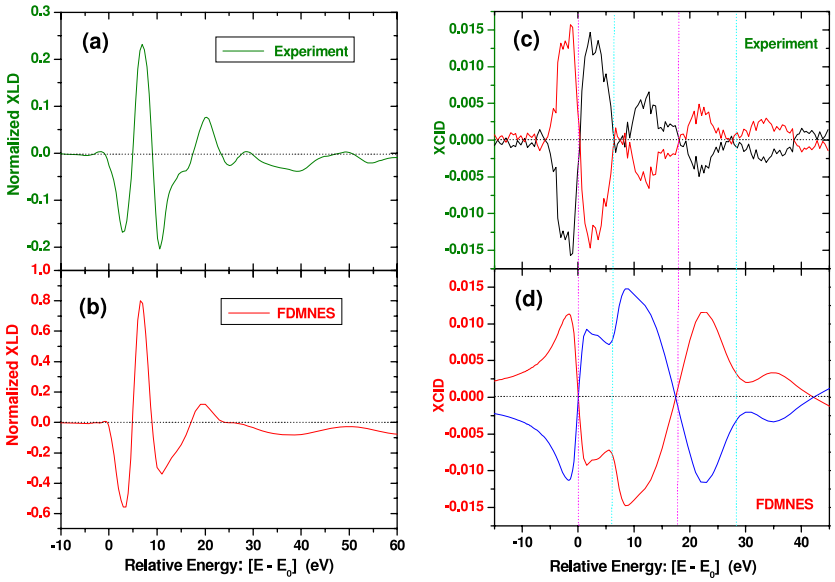

Figure 5. Comparison of the measured XLD spectrum of zincite (a) with an XLD spectrum simulated with the FDMNES code (b); both spectra were normalized with respect to the edge jump. Similarly, the measured XCID spectra (c) are compared with XCID spectra tentatively calculated with FDMNES (d); the XCID data displayed in (c) are the same as in figure 4(a) but we kept only the part of the signal that was fully inverted. All simulations were performed with the multiple-scattering option of the FDMNES code.

resolved by a fitting method, taking also into account a very weak drift arising from a small beam instability. The most serious difficulty in this analysis resulted from the presence of an unwanted Bragg glitch—marked with the arrow in figure 4(c)—that was found to spoil dramatically the end of the scan. This explains why the fitted amplitude of the XDOA signal (0.022) is smaller than the amplitude (0.027) we expected from the fully inverted part of the signal shown in figure 4(a). Anyhow, the fitted amplitude of natural XLD (0.138) is obviously large enough to mask completely the XDOA signal except for $\psi = \pm\pi/2$. Indeed, only a very small angular shift $\Delta\psi \simeq 0.2^\circ$ is enough to generate a significant residual XLD signal as discussed for figure 4(b).

3.4. Simulated XCID spectra

Since the XCID signal is only proportional to t_{113}, the extraction of the absolute value of this term is not a straightforward task. Actually, our strategy was to try to reproduce the XCID spectra using *ab initio* simulations carried out with the FDMNES code [69]. All calculations discussed below were performed in the standard multiple-scattering approach with muffin-tin-like potentials. The finite difference option of the FDMNES code would make it possible to get rid of the muffin-tin approximation but, unfortunately, at the expense of long computation times, which did not appear justified, at least in the early stage of the project. One has to realize, however, that reproducing dichroism spectra is considerably more difficult than simulating XANES spectra because we are concerned with differential effects, requiring a very accurate modellization of the relative amplitudes of the near-edge resonances. Another difficulty arose from the calculation of the simulated spectra as a function of a relative energy scale (E–E_0) in which E_0 refers to some arbitrary *muffin-tin* zero energy. This is why we found it highly desirable to compare first in figures 5(a) and (b) the experimental x-ray linear

dichroism spectrum displayed in figure 3(c) with the corresponding XLD spectrum calculated with FDMNES. Notice that both dichroism spectra were calculated from XANES spectra which were pre-normalized with respect to the edge jump. In the present simulation, the cluster centred around the absorbing atom included 122 atoms with a typical radius of $R \leqslant 6.9$ Å. In figure 5(a), which reproduces the experimental XLD spectrum, E_0 was carefully adjusted so as to let the relative energies of the strongest dichroism peak be identical in figures 5(a) and (b). Whereas nearly all characteristic features of the experimental spectrum of figure 5(a) can be identified as well in the simulated XLD spectrum, their relative amplitudes could not yet be reproduced accurately, partly due to excessive core–hole damping in the semiautomatic procedure used to convolute the calculated spectra.

In figures 5(c) and (d), we compare next the XCID spectra measured experimentally with XCID spectra simulated with FDMNES. The experimental data displayed in figure 5(c) are those of figure 4(a) but we deliberately kept only the part which is truly inverted for $\psi = \pm\pi/2$ because the latter part is the only one which can be assigned to the XDOA signal. For more clarity, E_0 was slightly shifted by 3.4 eV in order to match with the first zero of the XCID spectra. In figures 5(c) and (d), one may establish reasonable correlations between features that exist in both the experimental and in the simulated spectra but, obviously, the relative intensities are again poorly reproduced, especially in the central part of the spectrum (0–18 eV). Indeed, excessive core–hole damping will distort once again the XCID lineshapes over the whole spectral range, but this cannot explain such a strong alteration of the relative intensities of the XCID signatures in a narrow energy range. One is led therefore to envisage that something could be missing in our present calculation. We suspect that much of the discrepancy found between theory and experiment could stem from the neglect of multielectron excitations involving Zn 3d electrons given that their binding energy in hexagonal ZnO is only 10 eV [70]. This interpretation looks particularly relevant since the $E1E2$ matrix elements precisely involve final states mixing orbitals of p and d symmetry. Also the energy range where major spectral distortions are observed would be consistent with this interpretation, even though we admit that neither the FDMNES code nor the experiment allow us to determine unambiguously the Fermi level (E_F), that may be lying about 5 eV below E_0. Unfortunately, there is no theory available as yet to calculate $E1E2$ transition probabilities involving multiple electron excitations.

Nevertheless, this first result looks to us rather encouraging even though we completely realize that much time and effort will still be needed before one can reliably reproduce all features of the $E1E2$ spectra measured experimentally.

4. Open perspectives

For the first time, we produce clear experimental evidence that XCID spectra recorded near an absorption edge contain valuable information on the vector part of optical activity. We would like to focus first on the specific nature of the effective operator responsible for the XCID signatures and show that all types of measured XDOA, including XNCD, could be presented in a *unified* frame. We have already suggested elsewhere [16] that the effective operators of XDOA could be built from the tensor product ($\otimes$) of two spinless, time-reversal *odd* vector components, i.e. the orbital angular momentum $\mathbf{L}$ and the orbital anapole (toroidal) moment that is defined as $\mathbf{\Omega}_L = \frac{1}{2}(\mathbf{n}\times\mathbf{L} - \mathbf{L}\times\mathbf{n})$ in which $\mathbf{L}$ and the (electric) dipole $\mathbf{n} = \mathbf{r}/r$ are assumed to be orthogonal ($\mathbf{L}\cdot\mathbf{n} = 0$). The irreducible representations of $\mathbf{L}\otimes\mathbf{n}$ can be easily identified as

- a scalar part, $[\mathbf{L}\cdot\mathbf{\Omega}_L]^{(0)}$;
- a vector part, $[\frac{1}{2}(\mathbf{L}\times\mathbf{\Omega}_L - \mathbf{\Omega}_L\times\mathbf{L})]^{(1)} = L^2\cdot\mathbf{n}$;
- a *pseudo*-deviator part, $[\mathbf{\Omega}_L, \mathbf{L}]^{(2)}$.

The scalar part is relevant only for $E1M1$ excitations: the latter may induce a very weak XNCD signal that was measured very recently using enantiomorphous single crystals which were oriented in such a way that all $E1E2$ terms had to vanish [65]. Regarding XNCD experiments, though Natoli *et al* [13] were the first to derive an integral sum-rule to extract the *pseudo*-deviator operator responsible for XDOA, it is fair to recognize that the true physical content of this operator became clear only from the derivation given by Carra *et al* [66]. Regarding the vector part of OA, the effective operator is a polar vector ($L^2 \cdot \mathbf{n}$), which, as pointed out by Marri and Carra [54], may be responsible for ferroelectric order. Our result is entirely consistent with the old prediction made by Voigt [67] that crystal classes $4mm$, $3m$ and $6mm$ were suitable to observe pyroelectric properties. Note that, in this approach of OA, there is no place left for the octupolar operator of Marri–Carra, which is implicitly associated with the *symmetric* septor representation of $\mathrm{Re}[E1E2]_{\alpha,\beta\gamma}$: obviously, such a symmetric part is not related to OA.

Let us recall next that pyroelectric materials are systems in which a ferroelectric order can exist even in the absence of external electric field, and this order is expected to vary strongly with temperature. The thermal dependence of the pyroelectric coefficient of zincite is well known and was tentatively correlated in [26] with atomic displacements and anharmonic thermal vibrations. As far as the theory of Carra–Marri is correct, then one should expect the vector part of XDOA derived from the antisymmetric part of the $E1E2$ tensor to also be strongly temperature dependent: in this respect, it would be attractive to try to correlate directly the temperature dependences of XDOA and of the pyroelectric coefficient. As stressed by Albertsson *et al* [26], one should take into account in this problem not only the atomic displacements but eventually also a coupled redistribution of electronic charges with temperature. This points up the difficulty of using equation (7) in order to disentangle the contributions of the $E1E2$ and TMI third-rank tensors involved in resonant anomalous scattering. This remark does not necessarily contradict the conclusions of Collins *et al* regarding the temperature dependence of the forbidden (115) reflection of zincite [51] because the nature of their experiment was fundamentally different:

(i) from the corresponding diffraction geometry ($\theta_s \simeq 54.4°$; $\psi = 49.0°$) it appears as highly probable that the scattering intensity was largely dominated by the anisotropy of the electric dipole ($E1E1$) polarizability and therefore by the TMI contribution;
(ii) for that particular forbidden reflection, only the *symmetric* septor part of the $E1E2$ tensor is involved, which does not contribute to the vector part of optical activity;
(iii) numerical simulations carried out with FDMNES would suggest that the temperature dependence of the septor part should be rather weak [68].

In conclusion, we have shown that XCID measurements exploiting the *allowed* (300) reflection of zincite were a unique method to probe selectively the overlap of final states with either d or p symmetry in the conduction band of this crystal and ultimately in its valence band. Let us suggest that this method could be extended to a number of semiconductors featuring the same wurtzite-like structure, including numerous II–VI or III–V systems doped with transition metal ions and which are of considerable technological importance. In those systems in which the 3d (or 4d) band may be incompletely filled, it would be very attractive to try to correlate the strength of the local pyroelectric order and XDOA with the nature and amount of doping. In this perspective, let us emphasize that CID measurements in resonant inelastic x-ray scattering (RIXS) could be an interesting alternative experimental option to be considered. The expected advantages of XCID measurements in the RIXS regime would be that the Bragg angle (θ_s) could always be set to exactly 45°, whereas the two polarization components of the inelastically scattered photons could be easily resolved, e.g. with the RIXS spectrometer installed on the ESRF beamline ID12. Typically, the RIXS option would become particularly attractive for

crystals which do not exhibit such an intense reflection with a Bragg angle close to 45°, as was the case with the (300) reflection of zincite.

Acknowledgments

The authors are indebted to C Malgrange and E Kats for valuable comments. This work was part of a program supported by INTAS grant No 01-0822 under the coordination of J L Hodeau (CNRS, Grenoble).

References

[1] Buckingham A D 1968 *Adv. Chem. Phys.* **12** 107
[2] Barron L D 1982 *Molecular Light Scattering and Optical Activity* (Cambridge: Cambridge University Press)
[3] Graham E B and Raab R E 1992 *Phil. Mag.* **66** 269
[4] Arago D F M 1811 *Mém. Inst. France* 1 **12** 93
[5] Biot J B 1812 *Mém. Inst. France* 1 **13** 218
[6] O'Loane J K 1980 *Chem. Rev.* **80** 41
[7] Goulon J, Goulon-Ginet C, Rogalev A, Gotte V, Malgrange C, Brouder C and Natoli C R 1998 *J. Chem. Phys.* **108** 6394
[8] Alagna L, Prosperi T, Turchini S, Goulon J, Rogalev A, Goulon-Ginet C, Natoli C R, Peacock R D and Stewart B 1998 *Phys. Rev. Lett.* **80** 4799
[9] Stewart B, Peacock R D, Alagna L, Prosperi T, Turchini S, Goulon J, Rogalev A and Goulon-Ginet C 1999 *J. Am. Chem. Soc.* **121** 10233
[10] Goulon J, Goulon-Ginet C, Rogalev A, Benayoun G, Brouder C and Natoli C R 1999 *J. Synchrotron Radiat.* **6** 673
[11] Goulon J, Goulon-Ginet C, Rogalev A, Benayoun G, Malgrange C and Brouder C 1999 *Proc. SPIE* **3773** 316
[12] Goulon J, Goulon-Ginet C, Rogalev A, Benayoun G, Brouder C and Natoli C R 1999 *J. Synchrotron Radiat.* **7** 182
[13] Natoli C R, Brouder Ch, Sainctavit Ph, Goulon J, Goulon-Ginet Ch and Rogalev A 1998 *Eur. Phys. J.* B **4** 11
[14] Goulon J, Goulon-Ginet C, Rogalev A, Gotte V, Brouder C and Malgrange C 1999 *Eur. Phys. J.* B **12** 373
[15] Goulon J, Rogalev A, Wilhelm F, Jaouen N, Goulon-Ginet Ch and Brouder Ch 2003 *J. Phys.: Condens. Matter* **15** S633
[16] Goulon J, Rogalev A, Wilhelm F, Jaouen N, Goulon-Ginet Ch, Carra P, Marri I and Brouder Ch 2003 *J. Exp. Theor. Phys.* **97** 402
[17] Jerphagnon J and Chemla D 1976 *J. Chem. Phys.* **65** 1522
[18] Landau L D and Lifshitz E M 1960 *Electrodynamics of Continuous Media* (Oxford: Pergamon)
[19] Voigt W 1905 *Ann. Phys., Lpz.* **18** 651
[20] Fedorov F I 1959 *Opt. Spectrosc.* **6** 237
[21] Ivchenko E L, Permogorov S A and Sel'kin A V 1978 *JETP Lett.* **27** 24
Ivchenko E L, Permogorov S A and Sel'kin A V 1978 *Solid State Commun.* **28** 345
[22] Mashlyatina T M, Nedzvetskii D S and Sel'kin A V 1978 *JETP Lett.* **27** 539
[23] Ivchenko E L and Sel'kin A V 1979 *Sov. Phys.—JETP* **49** 933
[24] Graham E B and Raab R E 1990 *Proc. R. Soc.* A **430** 593
[25] Graham E B and Raab R E 1996 *J. Opt. Soc. Am.* A **13** 1239
[26] Albertsson J, Abrahams S C and Kvick Å 1989 *Acta Crystallogr.* B **45** 34
[27] Graham E B and Raab R E 1997 *J. Opt. Soc. Am.* A **14** 131
[28] Barron L D and Gray C G 1973 *J. Phys. A: Math. Gen.* **6** 59
[29] Templeton D H and Templeton L K 1982 *Acta Crystallogr.* A **38** 62
Templeton D H and Templeton L K 1985 *Acta Crystallogr.* A **41** 133
[30] Templeton D H and Templeton L K 1994 *Phys. Rev.* B **49** 14850
[31] Templeton D H 1998 *Acta Crystallogr.* A **54** 158
[32] Kirfel A, Petcov A and Eichhorn K 1991 *Acta Crystallogr.* A **47** 180
[33] Kirfel A and Petcov A 1992 *Acta Crystallogr.* A **48** 247
[34] Kirfel A and Morgenroth W 1993 *Acta Crystallogr.* A **49** 35
[35] Finkelstein K D, Qun S and Shastri S 1992 *Phys. Rev. Lett.* **69** 1612
[36] Dmitrienko V E 1983 *Acta Crystallogr.* A **39** 29
Dmitrienko V E 1984 *Acta Crystallogr.* A **40** 89

[37] Belyakov V A and Dmitrienko V E 1989 *Sov. Phys.—Usp.* **32** 697
[38] Ovchinnikova E N and Dmitrienko V E 1997 *Acta Crystallogr.* A **53** 388
[39] Dmitrienko V E and Ovchinnikova E N 2000 *Acta Crystallogr.* A **56** 340
Dmitrienko V E and Ovchinnikova E N 2001 *Acta Crystallogr.* A **57** 642
[40] Ovchinnikova E N, Oreshko A P, Joly Y, Kirfel A, Tolochko B P and Dmitrienko V E 2005 *Phys. Scr.* T **115** 252
[41] Blume M 1985 *J. Appl. Phys.* **57** 3615
[42] Blume M 1994 *Resonant Anomalous X-ray Scattering* ed G Materlik, C J Sparks and K Fischer (Amsterdam: North-Holland) p 495
[43] Jerphagnon J, Chemla D and Bonneville R 1978 *Adv. Phys.* **27** 609
[44] Lee T L, Felici R, Hirano K, Cowie B, Zegenhagen J and Colella R 2001 *Phys. Rev.* B **64** 201316R
[45] Elfimov I S, Skorikov N A, Anisimov V I and Sawatzky G A 2002 *Phys. Rev. Lett.* **88** 015504
[46] Kokubun J, Kanazawa M, Ishida K and Dmitrienko V E 2001 *Phys. Rev.* B **64** 073203
[47] Kirfel A, Grybos J and Dmitrienko V E 2002 *Phys. Rev.* B **66** 165202
[48] Detlefs C 2004 *Physica* B **345** 45
[49] Mazzoli C, Wilkins S B, Di Matteo S, Detlefs B, Detlefs C, Scagnoli V, Paolasini L and Ghigna P 2006 *Preprint* cond-mat/0611239v1
[50] Thoma K, Dorner B, Duesing G and Wegener W 1974 *Solid State Commun.* **15** 1111
[51] Collins S P, Laundy D, Dmitrienko V E, Mannix D and Thompson P 2003 *Phys. Rev.* B **68** 064110
[52] Luo J, Trammell G T and Hannon J P 1993 *Phys. Rev. Lett.* **71** 287
[53] Carra P and Thole B T 1994 *Rev. Mod. Phys.* **66** 1509
[54] Marri I and Carra P 2004 *Phys. Rev.* B **69** 113101
[55] Buckingham A D and Raab R E 1975 *Proc. R. Soc.* A **345** 365
[56] Birss R R 1963 *Rep. Prog. Phys.* **26** 307
[57] Goulon J, Rogalev A, Gauthier C, Goulon-Ginet C, Pasté S, Signorato R, Neuman C, Varga L and Malgrange C 1998 *J. Synchrotron Radiat.* **5** 232
[58] Rogalev A, Goulon J, Goulon-Ginet C and Malgrange C 2001 *Magnetism and Synchrotron Radiation* (*Springer Lecture Notes in Physics* vol 565) ed E Beaurepaire *et al* (Berlin: Springer) p 60
[59] Neumann C, Rogalev A, Goulon J, Lingham M and Ziegler E 1998 *J. Synchrotron Radiat.* **5** 998
[60] Jaouen N, Wilhelm F, Rogalev A, Goulon J and Tonnerre J M 2004 *AIP Conf. Proc.* **705** 1134
[61] Goulon J, Goulon-Ginet Ch and Gotte V 2000 *X-ray Absorption Spectroscopy Applied to Porphyrin Chemistry* (*The Porphyrin Handbook* vol 7) ed K M Kadish, K M Smith and R Guilard (New York: Academic) p 79
[62] James F and Roos M 1987 *MINUIT Program* Program Library No D506, CERN Computer Center
[63] Sève L, Tonnerre J M and Raoux D 1998 *J. Appl. Crystallogr.* **31** 700
[64] Goulon J, Rogalev A, Goujon G, Gauthier C, Moguiline E, Solé A, Feite S, Wilhelm F, Jaouen N, Goulon-Ginet C, Dressler P, Rohr P, Lampert M O and Henck R 2005 *J. Synchrotron Radiat.* **12** 57
[65] Rogalev A, Bossak A, Goulon J and Wilhelm F 2007 in preparation
[66] Carra P, Jerez A and Marri I 2003 *Phys. Rev.* B **67** 045111
[67] Voigt W 1910 *Lehrbuch Der Kristallphysik* (Leipzig: Teubner)
[68] Dmitrienko V E, Ovchinnikova E N, Ishida K, Kokubun J, Kirfel A, Collins S P, Laundy D, Oreshko A P and Cabaret D 2004 *Phys. Status Solidi* c **1** 3081
[69] Joly Y 2001 *Phys. Rev.* B **63** 125120
[70] Jaffe J E, Pandey R and Kunz A B 1991 *Phys. Rev.* B **43** 14030